Rapid Communications

$CeAu_2Bi$: A new nonsymmorphic antiferromagnetic compound

M. M. Piva,[1,2,*] W. Zhu,[2,3] F. Ronning,[2] J. D. Thompson,[2] P. G. Pagliuso,[1] and P. F. S. Rosa[2]

[1]*Instituto de Física "Gleb Wataghin", UNICAMP, 13083-859, Campinas, SP, Brazil*

[2]*Los Alamos National Laboratory, Los Alamos, New Mexico 87545, USA*

[3]*Institute of Natural Sciences, Westlake Institute of Advanced Study and School of Science, Westlake University, Hangzhou, 310024, China*

(Received 18 February 2019; published 23 July 2019)

Here, we report the structural and electronic properties of $CeAu_2Bi$, a new heavy-fermion compound crystallizing in a nonsymmorphic hexagonal structure ($P63/mmc$). The Ce^{3+} ions form a triangular lattice which orders antiferromagnetically below $T_N = 3.1$ K with a magnetic hard axis along the c axis. Under applied pressure, T_N increases linearly at a rate of 0.07 K/kbar, indicating that the Ce f electrons are fairly localized. In fact, heat capacity measurements provide an estimate of 150(10) mJ/mol K^2 for the Sommerfeld coefficient. The crystal-field scheme obtained from our thermodynamic data points to a ground state with a dominantly $|j_z = \pm 1/2\rangle$ character, which commonly occurs in systems with a hard c axis. Finally, electronic band structure calculations and symmetry analysis in k space reveal that $CeAu_2Bi$ hosts symmetry-protected crossings at $k_z = \pi$ in the paramagnetic state.

DOI: 10.1103/PhysRevMaterials.3.071202

I. INTRODUCTION

Materials discovery is an important part of condensed matter research and is driven by the possibility of finding materials that may host new physical phenomena and enable future technologies. Recently, compounds with topologically protected surface states are being extensively pursued due to their potential applications. Though topology concepts have been extended to condensed matter physics, they remain rather unexplored in $4f$ cerium-based materials [1–4]. Many of these materials crystallize in nonsymmorphic structures, which are predicted to generate protected band crossings as well as surface states [5–8]. In addition, Ce-based materials often display emergent properties such as complex magnetism and unconventional superconductivity, and the interplay between topology and emergence could lead to new quantum states of matter. Nonsymmorphic topological insulators were predicted to host surface fermions, which exhibit an "hourglass"-shaped dispersion [6,9–12]. Recent experiments in KHgSb provide experimental evidence of such fermions [13]. Further, nonsymmorphic symmetries may produce band touching, hindering the formation of a gapped insulator. As a result, a nodal semimetal ground state is realized in which band degeneracies are required by symmetry. Hexagonal space groups are notable for their sixfold screw rotation symmetry which leads to multiple band crossings with an "accordionlike" dispersion [8]. UPt_3, for instance, crystallizes in the same nonsymmorphic hexagonal space group as KHgSb, $P63/mmc$ [space group (SG) No. 194], and may be a topological superconductor [14]. In fact, hexagonal materials in space groups containing both inversion and glide mirror symmetries are predicted to host symmetry-protected band crossings, pinned to a high-symmetry plane $k_z = \pi$ [8]. Therefore, materials that crystallize in the $P63/mmc$ (SG No. 194) structure are promising to display nontrivial topology features.

Here, we report the electronic and structural properties of the new Ce-based compound $CeAu_2Bi$ that also crystallizes in the $P63/mmc$ hexagonal structure. Single crystals of $CeAu_2Bi$ and $LaAu_2Bi$ were grown by the Bi-flux technique as described in the Supplemental Material along with other experimental details [15]. As we will show, $CeAu_2Bi$ is a moderately heavy-fermion compound that orders antiferromagnetically below 3.1 K out of a $|j_z = \pm 1/2\rangle$ crystal-field doublet. Though applied pressure increases the ordering temperature, a field of 4.5 T applied perpendicular to the c axis is sufficient to suppress long-range order, similar to $CePd_2In$ [16–21]. Finally, motivated by predictions of band crossings at high-symmetry planes [8], we also present the calculated band structure of $CeAu_2Bi$, which reveals a symmetry-protected band crossing at $k_z = \pi$ as well as other trivial bands at E_F. These electronic structure calculations along with experiments support the possibility that $CeAu_2Bi$ is a moderately correlated antiferromagnet (AFM) that may host a nontrivial electronic topology. Our experimental data, however, do not provide evidence for the predicted topological states as trivial bands overwhelm the electronic response at E_F.

II. RESULTS

Figure 1(a) shows the hexagonal crystal structure shared by $CeAu_2Bi$ and $LaAu_2Bi$. In this structure, Ce/La planes are separated by AuBi layers. Figure 1(b) presents the triangular lattice formed by Ce^{3+} ions. The crystallographic data of both compounds are summarized in Table I in the Supplemental Material [15]. Both compounds crystallize in the hexagonal $P63/mmc$ nonsymmorphic structure, although $CeAu_2Bi$ has a slightly smaller unit cell than $LaAu_2Bi$, as expected from the lanthanide series contraction. There is no detectable second phase in single-crystal diffraction, though a small ($<5\%$)

*mpiva@ifi.unicamp.br

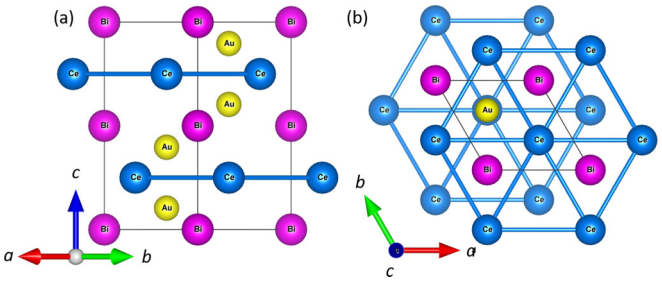

FIG. 1. (a) Hexagonal structure of $CeAu_2Bi$, $a = 4.887(1)$ Å and $c = 9.375(1)$ Å. (b) A c-axis view of the crystalline structure of $CeAu_2Bi$ displaying the triangular lattice formed by Ce^{3+} ions.

amount of impurity phases cannot be ruled out, and indeed there is evidence for a Au_2Bi impurity phase in both $CeAu_2Bi$ and $LaAu_2Bi$ in resistivity measurements (see Supplemental Material for more details [15]).

Figure 2(a) shows the magnetic susceptibility (χ) as a function of temperature at $\mu_0 H = 0.1$ T applied parallel and perpendicular to the c axis of $CeAu_2Bi$. These measurements find that the c axis is the hard axis and that Ce^{3+} moments order antiferromagnetically at $T_N = 3.1$ K, as we can clearly see in the top inset of Fig. 2(a). The bottom inset shows the inverse of χ after subtraction of a Pauli contribution [$\chi_0 \approx 0.4 \times 10^{-3}$ emu/(mol Oe)] for $H \parallel c$, $H \perp c$, and for

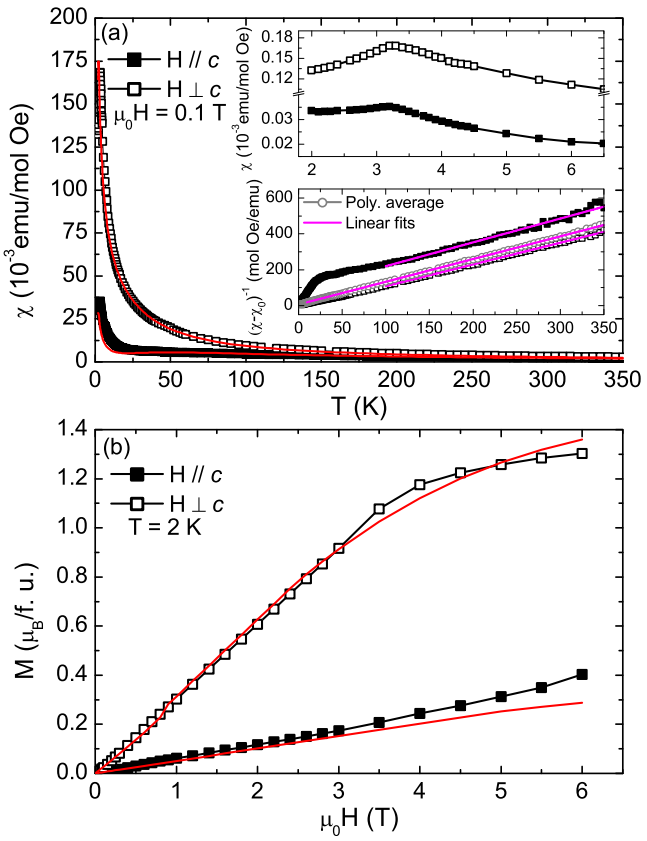

FIG. 2. (a) $\chi(T)$ at $\mu_0 H = 0.1$ T. The top inset shows a zoomed-in view of $\chi(T)$ in the low-temperature range. The bottom insets show $(\chi - \chi_0)^{-1}$ as a function of temperature. (b) M as a function of applied magnetic field. The solid red lines are fits using a CEF mean-field model.

the polycrystalline average ($\frac{1}{3}\chi_{||c} + \frac{2}{3}\chi_{\perp c}$). By performing linear fits in the high-temperature range, we extract the following Ce^{3+} effective moments: $\mu_{\text{eff}} = 2.57(1)\mu_B$, when $H \perp c$, $\mu_{\text{eff}} = 2.46(2)\mu_B$ for $H \parallel c$, and $\mu_{\text{eff}} = 2.52(1)\mu_B$ for the polycrystalline average. These values are close to the calculated value of $2.54\mu_B$ for a free Ce^{3+} ion. From these fits, we find Curie-Weiss temperatures of $\theta_{\text{CW}} = 10(1)$ K with $H \perp c$, $\theta_{\text{CW}} = -67(4)$ K with $H \parallel c$, and $\theta_{\text{CW}} = -5.5(2)$ K from the polycrystalline average. Assuming that crystalline electrical field (CEF) effects dominate θ_{CW}, we consider the polycrystalline average to calculate the frustration parameter ($f = |\theta_{\text{CW}}|/T_N$) of around 1.8, which indicates that only weak geometrical frustration is present in $CeAu_2Bi$. At low temperatures, one can see a deviation from the Curie-Weiss behavior when $H \parallel c$, which is likely associated with crystal-field effects, as we will discuss below.

Figure 2(b) displays the magnetization (M) behavior as a function of applied magnetic field at 2 K. For $H \perp c$, M starts to saturate at 3.5 T, pointing to a fully polarized spin state at higher fields. In fact, the saturated moment of $\approx 1.3\mu_B$ is expected for a $|j_z = \pm 1/2\rangle$ doublet ground state in hexagonal symmetry, in agreement with Ref. [22] and similar to $CeAgSb_2$ [23]. For $H \parallel c$ the magnetization increases monotonically with field.

Figure 3(a) displays the specific heat divided by the temperature (C_p/T) for both $CeAu_2Bi$ and $LaAu_2Bi$ as a function of temperature. $CeAu_2Bi$ displays a lambda-type peak at 3.1 K which characterizes T_N and is in agreement with $\chi(T)$ results. Moreover, the insets of Fig. 3(a) plot C_p/T as a function of T^2 for both compounds. The solid line in the left inset is a linear fit that gives the Sommerfeld coefficient (γ) of 2.4(2) mJ/(mol K^2) for $LaAu_2Bi$. An extrapolation to $T = 0$ K of a linear fit between 5 and 15 K of C_p/T vs T^2 above T_N (right inset) gives an estimated $\gamma = 150(10)$ mJ/(mol K^2) for $CeAu_2Bi$, that characterizes it as a moderately heavy-fermion compound. By subtracting the phonon contribution for the specific heat of $CeAu_2Bi$ assumed to be given by the specific heat of its nonmagnetic analog $LaAu_2Bi$, we obtain the magnetic specific heat that is displayed in Fig. 3(b). The integral of C_{mag}/T vs T gives the magnetic entropy of $CeAu_2Bi$, which is plotted in the inset of Fig. 3(b) and reaches 80% of the doublet entropy $R\ln(2)$ at T_N. The presence of magnetic entropy above T_N could arise from a partial Kondo effect but also from short-range magnetic correlations. C_p/T as a function of temperature for $CeAu_2Bi$ at different applied magnetic fields is displayed in Fig. 3(c). Similar to $CePd_2In$ [20], T_N is suppressed as a function of increasing field, being fully suppressed at 4.5 T and in agreement with our magnetization data.

The solid red lines in the main panels of Figs. 2(a) and 2(b) and in Fig. 3(b) are fits to data using a CEF mean-field model considering anisotropic nearest-neighbor interactions and the hexagonal CEF Hamiltonian: $\mathcal{H} = z_i J_i J \cdot \langle J \rangle + B_2^0 O_2^0 + B_4^0 O_4^0 + B_6^0 O_6^0 + B_6^6 O_6^6$. $z_i J_i$ represents interactions (i = AFM, FM) between nearest neighbors that mimic the Ruderman-Kittel-Kasuya-Yosida (RKKY) interaction, B_n^m are the CEF parameters, and the O_n^m are the Steven's operators, similar to the approach used in Refs. [24,25]. By simultaneously performing fits to $\chi(T)$, $M(H)$, and $C_p(T)$

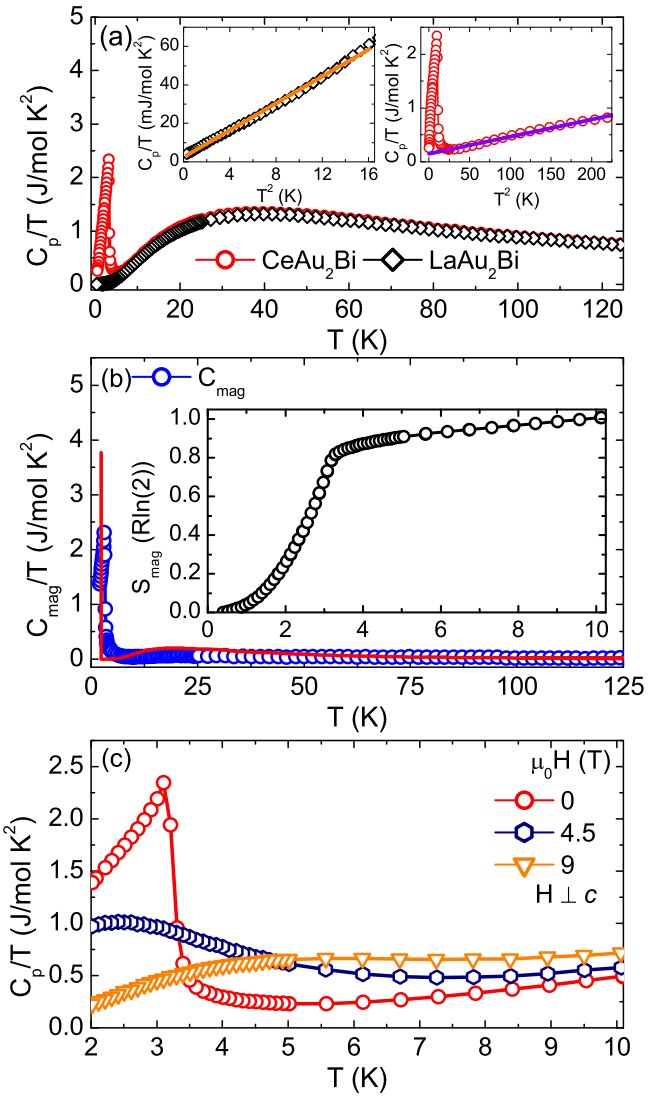

FIG. 3. (a) Specific heat measurements for CeAu$_2$Bi and LaAu$_2$Bi. The insets show C_p/T as a function of T^2. The solid line is an extrapolation of the fit used to extract the Sommerfeld coefficient. (b) Magnetic specific heat and entropy of CeAu$_2$Bi. The solid red line is a fit using a CEF mean-field model. (c) Specific heat behavior as a function of temperature of CeAu$_2$Bi for several applied magnetic fields.

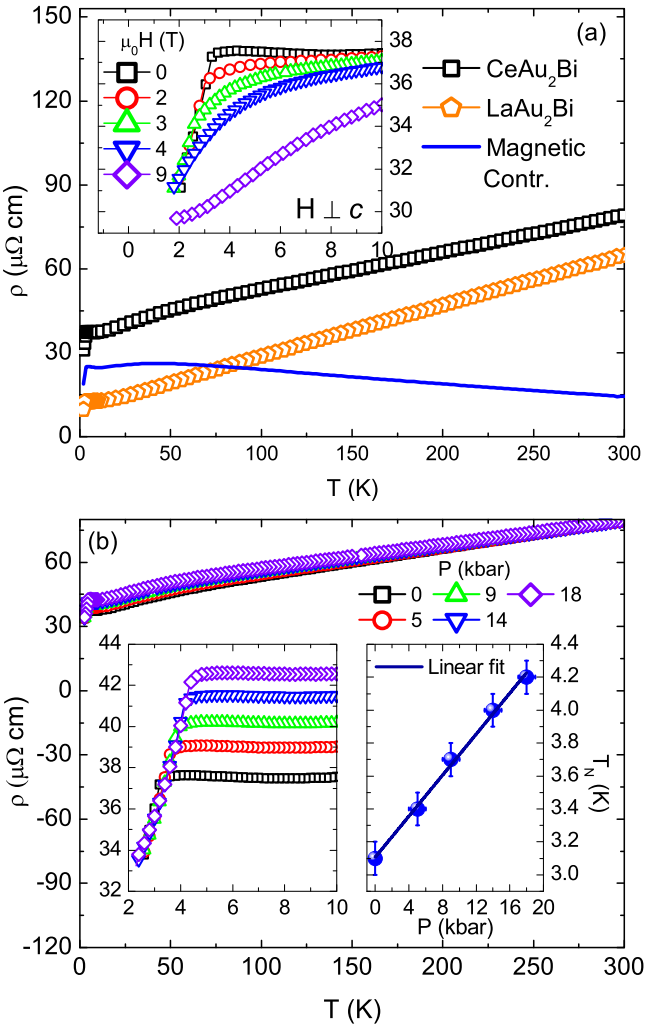

FIG. 4. (a) $\rho(T)$ for CeAu$_2$Bi and LaAu$_2$Bi. The inset shows the low-temperature behavior of the CeAu$_2$Bi resistivity for several applied magnetic fields. (b) $\rho(T)$ of CeAu$_2$Bi for different applied pressures. The insets show the low-temperature range of the resistivity for several applied pressures and the temperature-pressure phase diagram, respectively.

data, we extract the CEF scheme and two RKKY parameters for this compound. For the RKKY parameters we obtain $z_{\mathrm{AFM}}J_{\mathrm{AFM}} = 0.78$ K and $z_{\mathrm{FM}}J_{\mathrm{FM}} = -0.20$ K. We note that the extracted $T_N \approx 2.3$ K is slightly smaller than the experimental value, which could be due to additional exchange interactions not captured by our simple mean-field model. For the CEF parameters we obtained the following values: $B_2^0 \approx 7.28$ K, $B_4^0 \approx -0.04$ K, $B_6^0 \approx 0.03$ K, and $B_6^6 \approx -0.01$ K. These parameters imply a ground state composed of a Γ_6 doublet ($|\pm 1/2\rangle$), a first excited state $|\pm 3/2\rangle$ doublet at 60 K, and a second excited state $|\pm 5/2\rangle$ doublet at 130 K. We note that the CEF parameters acquired from fits of macroscopic data may not be fully accurate or unique. Therefore, to unambiguously determine the CEF scheme, inelastic neutron scattering and x-ray absorption experiments should be performed.

Figure 4(a) displays the electrical resistivity (ρ) of CeAu$_2$Bi, LaAu$_2$Bi, and the magnetic resistivity [ρ(CeAu$_2$Bi) − ρ(LaAu$_2$Bi)]. CeAu$_2$Bi displays metallic behavior but with a rather poor relative resistance ratio $R(300\ \mathrm{K})/R(2\ \mathrm{K}) \approx 2.5$. Presently, we do not know if this ratio is intrinsic or possibly due to weak site disorder. Nevertheless, there is a well-defined kink around 3.1 K that reflects the loss of spin-disorder scattering below T_N. Near 50 K there is a broad hump in magnetic resistivity that is most likely associated with the depopulation of the first excited crystal-field state. In the inset of Fig. 4(a) we plot the field dependence of $\rho(T)$ with $H \perp c$ near T_N. For fields higher than 3 T, T_N can no longer be identified above 1.8 K, in agreement with the specific heat measurements and similar to CePd$_2$In [20]. Moreover, in the Fermi-liquid state at 9 T where ρ increases as T^2, the coefficient of the T^2 term is $A = 0.10(1)\ \mu\Omega\,\mathrm{cm/K^2}$. This value of A implies a γ of 100(20) mJ/(mol K^2) considering the Kadowaki-Woods ratio [26] and is in good agreement with the coefficient extracted

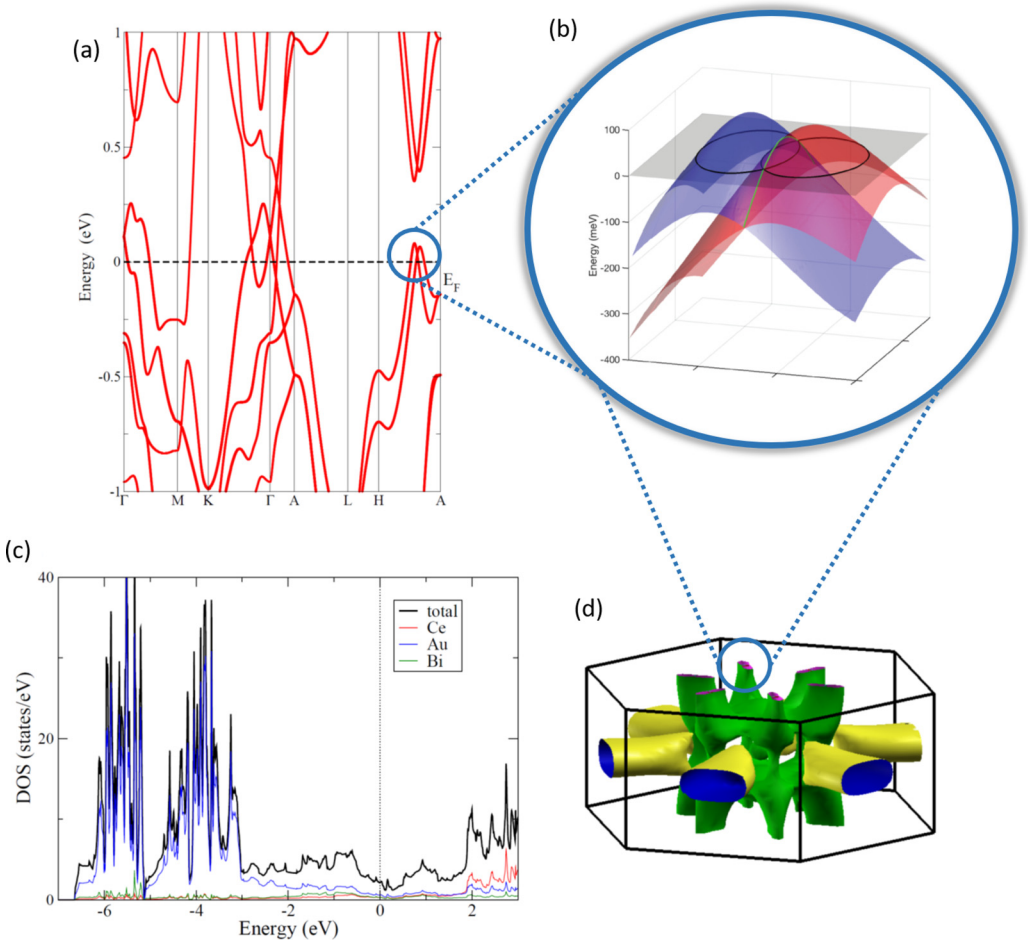

FIG. 5. (a) Electronic band structure of $CeAu_2Bi$. (b) Zoom-in view of the electronic structure for $k_z = \pi$. Two bands with opposite R-z eigenvalues (red and blue) intersect forming a line (green), which intersects the chemical potential (gray plane) at the two points where the Fermi surfaces of the individual bands (black circles) intersect (see text for details). (c) Density of states and (d) Fermi surface of $CeAu_2Bi$.

from specific heat measurements. $LaAu_2Bi$ also displays metallic behavior at high temperatures, whereas at low temperatures a downturn is observed near 2 K, likely due to the superconducting transition of the extrinsic binary Au_2Bi at 1.8 K [15,27], as no evidence of superconductivity was found in specific heat measurements. Figure 4(b) presents $\rho(T)$ of $CeAu_2Bi$ at several applied pressures. At high temperatures, $CeAu_2Bi$ displays metallic behavior for all pressures. The left inset in Fig. 4(b) displays the pressure dependence of the $\rho(T)$, and the right inset shows the linear increase of T_N with pressure at a rate of 0.069(1) K/kbar. The increase of T_N with pressure within the Doniach diagram further supports the localized nature of the f electrons in $CeAu_2Bi$.

To explore the possibility that $CeAu_2Bi$ might present a nontrivial electronic structure and to place experimental results in the broader context of its global electronic structure, we perform *ab initio* calculations based on density functional theory [28–30]. We compute the band structure of $CeAu_2Bi$ with spin-orbit coupling and considering the Ce $4f$ electron localized in the core, as illustrated in Fig. 5(a). Because the magnetic structure is unknown we also consider the nonmagnetic solution relevant for the paramagnetic state above T_N, as well as the nonmagnetic La analog. Let us consider each of the high-symmetry lines. All bands in Fig. 5(a) are at least doubly degenerate because the crystal structure has inversion symmetry $\hat{P}$ and (neglecting magnetic order) time-reversal symmetry $\hat{T}$, which ensures that the bands are Kramers degenerate for all $\mathbf{k}$ [31]. At any wave vector along the $k_z = 0$ plane, bands avoid crossing at all momenta, whereas in the $k_z = \pi$ plane, the band structure shows crossings along the H-A line. Symmetry analysis indicates that this crossing is attributed to the nonsymmorphic symmetry $R_z : (x, y, z) \to (x, y, -z + c/2)$, $(s_x, s_y, s_z) \to (-s_x, -s_y, s_z)$, where R_z is a symmetry combining a twofold screw axis along the z direction and inversion symmetry. Importantly, we find that $R_z * (P * T) = e^{-ik_z}(P * T) * R_z$. On the mirror invariant planes $k_z = 0$ and $\pm\pi$, the bands can be labeled by their R_z eigenvalues $\pm i$ because $R_z^2 = -1$. This means that the degenerate bands on the $k_z = 0$ plane have opposite R_z eigenvalues $(i, -i)$, and two sets of such doublet bands generally anticross, i.e., bands with the same R_z eigenvalues avoid crossing. At $k_z = \pi$, however, the degenerate bands have the same R_z eigenvalue $\pm(i, i)$. In this case, two doublet bands with opposite R_z eigenvalues may cross, creating a symmetry-protected four-band crossing line [32,33]. In Fig. 5(b), we show a zoom-in figure revealing the crossing bands whose intersection passes through the chemical potential. One can see that the protected band crossings create a line (green solid line) that extends

in a direction perpendicular to H-A. This line does form a ring about the A point but is in fact intersected by the fourfold band degeneracy along A-L and symmetry equivalent directions. Away from the $k_z = \pi$ plane, R_z is no longer a good symmetry and the bands hybridize, opening a gap. Although it is exciting to find a symmetry-protected crossing intersecting the Fermi energy in an f-electron system, we note that there exist multiple trivial Fermi surface sheets [Fig. 5(d)], which likely dominate the transport and thermodynamic properties of this compound. Furthermore, our density functional theory (DFT) calculations do not consider the presence of heavy electrons and antiferromagnetic order. The former would require DFT+DMFT (dynamical mean-field theory) calculations to take correlations into account more precisely. The latter would require the determination of the magnetic structure, which is beyond the scope of the present work.

At the $k_z = \pi$ plane, the band structure shows fourfold degeneracy along the A-L line. This higher-level degeneracy results from the mirror symmetry $M_y : (x, y, z) \mapsto (x, -y, z)$. The implication is that the high-symmetry path $k_y = 0$ at $k_z = \pi$ is just the intersecting line of the invariant plane $k_y = 0$ of M_y and the invariant plane $k_z = \pi$ of R_z. On this invariant line, the action of $\mathbf{M}_y$ will transform the eigenstate into a partner of an opposite R_z label, which then relates the two Kramers pairs and ensures a fourfold degeneracy. In Fig. 5(c) we show the calculated density of states for $CeAu_2Bi$. Extracting the Sommerfeld coefficient from this density of states yields a γ of 2.6(3) $\mathrm{mJ/(mol\,K^2)}$. This value is in good agreement with the γ of 2.4(2) $\mathrm{mJ/(mol\,K^2)}$ experimentally found for $LaAu_2Bi$, i.e., the $4f$ localized limit of $CeAu_2Bi$. Finally, Fig. 5(d) displays the Fermi surface of $CeAu_2Bi$, which is sixfold symmetric and presents two-dimensional (2D)-like cylindrical pockets, along with 3D-like pockets.

III. CONCLUSIONS

In summary, we report the electronic and structural properties of the new heavy-fermion compound $CeAu_2Bi$ and of its nonmagnetic analog $LaAu_2Bi$, which crystallize in the nonsymmorphic $P63/mmc$ hexagonal structure. At high temperatures, both samples show metallic behavior. At low temperatures, $CeAu_2Bi$ orders antiferromagnetically below 3.1 K with a magnetic hard axis along the c axis. The antiferromagnetic transition recovers 80% of $R\ln(2)$, indicating that the Ce^{3+} local moments are fairly localized in this compound. Specific heat measurements and the Kadawoki-Woods ratio estimate a Sommerfeld coefficient of 120(40) $\mathrm{mJ/(mol\,K^2)}$ in the paramagnetic state, placing $CeAu_2Bi$ as a moderately heavy compound. Furthermore, by performing fits of $\chi(T)$, $M(H)$, and $C_p(T)$ using a CEF mean-field model, we could extract two competing exchange interactions, $z_{\mathrm{AFM}}J_{\mathrm{AFM}} = 0.8$ K and $z_{\mathrm{FM}}J_{\mathrm{FM}} = -0.2$ K, and a Γ_6 ($j_z = |\pm 1/2\rangle$) ground state. Moreover, electrical resistivity experiments under pressure revealed an increase of T_N as a function of pressure reaching a maximum of 4.2 K at 18 kbar. Neutron diffraction experiments would be useful to solve the magnetic structure and to probe the CEF scheme of this new compound. Also, experiments at higher pressures are needed to investigate whether T_N can be suppressed and a quantum critical point can be achieved in $CeAu_2Bi$. Finally, to shed new light on the electronic energy levels of $CeAu_2Bi$, we performed *ab initio* calculations based on the density functional theory. These calculations show that at the $k_z = 0$ plane, the band structure has twofold degeneracy and bands avoid crossing at all momenta. At $k_z = \pi$, the band structure is fourfold degenerate along the A-L line and possesses multiple band crossings elsewhere in the $k_z = \pi$ plane, one of which intersects the Fermi energy. However, no experimental evidence of band crossings was observed in our measurements. In this regard, angle-resolved photoemission spectroscopy (ARPES) experiments would be useful to directly probe the electronic bands, search for band crossings, and to determine the influence of magnetism on such topological band crossings.

ACKNOWLEDGMENTS

We would like to acknowledge N. Harrison and M. Rahn for useful discussions. Sample synthesis and crystal structure determination were supported by the DOE BES "Science of 100 Tesla" project. Physical property measurements and band structure calculations were supported by the DOE BES "Quantum Fluctuations in Narrow-Band Systems" project. M.M.P. acknowledges support from the Sao Paulo Research Foundation (FAPESP) Grants No. 2015/15665-3, No. 2017/25269-3, and No. 2017/10581-1, CAPES and CNPq, Brazil. W.Z. thanks the startup funding from Westlake University. Scanning electron microscope and energy dispersive x-ray measurements were performed at the Center for Integrated Nanotechnologies, an Office of Science User Facility operated for the U.S. Department of Energy (DOE) Office of Science.

[1] L. M. Schoop, A. Topp, J. Lippmann, F. Orlandi, L. Müchler, M. G. Vergniory, Y. Sun, A. W. Rost, V. Duppel, M. Krivenkov, S. Sheoran, P. Manuel, A. Varykhalov, B. Yan, R. K. Kremer, C. R. Ast, and B. V. Lotsch, Sci. Adv. **4**, eaar2317 (2018).

[2] G. Chang, B. Singh, S.-Y. Xu, G. Bian, S.-M. Huang, C.-H. Hsu, I. Belopolski, N. Alidoust, D. S. Sanchez, H. Zheng, H. Lu, X. Zhang, Y. Bian, T.-R. Chang, H.-T. Jeng, A. Bansil, H. Hsu, S. Jia, T. Neupert, H. Lin, and M. Z. Hasan, Phys. Rev. B **97**, 041104(R) (2018).

[3] C. Guo, C. Cao, M. Smidman, F. Wu, Y. Zhang, F. Steglich, F.-C. Zhang, and H. Yuan, npj Quantum Mater. **2**, 39 (2017).

[4] S. Dzsaber, L. Prochaska, A. Sidorenko, G. Eguchi, R. Svagera, M. Waas, A. Prokofiev, Q. Si, and S. Paschen, Phys. Rev. Lett. **118**, 246601 (2017).

[5] S. Parameswaran, A. Turner, D. Arovas, and A. Vishwanath, Nat. Phys. **9**, 299 (2013).

[6] K. Shiozaki, M. Sato, and K. Gomi, Phys. Rev. B **93**, 195413 (2016).

[7] S.-Y. Yang, H. Yang, E. Derunova, S. S. P. Parkin, B. Yan, and M. N. Ali, Adv. Phys.: X **3**, 1414631 (2017).

[8] J. Zhang, Y.-H Chan, C.-K Chiu, M. G. Vergniory, L. M. Schoop, and A. P. Schnyder, Phys. Rev. Mater. **2**, 074201 (2018).

[9] Z. Wang, A. Alexandradinata, R. J. Cava, and B. A. Bernevig, Nature (London) **532**, 189 (2016).
[10] A. Alexandradinata, Z. Wang, and B. A. Bernevig, Phys. Rev. X **6**, 021008 (2016).
[11] P.-Y. Chang, O. Erten, and P. Coleman, Nat. Phys. **13**, 794 (2017).
[12] B. J. Wieder, B. Bradlyn, Z. Wang, J. Cano, Y. Kim, H.-S. D. Kim, A. M. Rappe, C. L. Kane, and B. A. Bernevig, Science **361**, 246 (2018).
[13] J. Ma *et al.*, Sci. Adv. **3**, e1602415 (2017).
[14] Y. Yanase and K. Shiozaki, Phys. Rev. B **95**, 224514 (2017).
[15] See Supplemental Material at http://link.aps.org/supplemental/10.1103/PhysRevMaterials.3.071202 for the computational and experimental details, the crystallographic data of both compounds, the detailed EDX spectra for $CeAu_2Bi$ and the low temperature resistivity for both compounds.
[16] B. Xue, F. Hulliger, C. Baerlocher, and M. Estermann, J. Alloys Compd. **191**, L9 (1993).
[17] S. Mock, T. Pietrus, A. Sidorenko, R. Vollmer, and H. v. Löhneysen, J. Low Temp. Phys. **104**, 95 (1996).
[18] A. D. Bianchi, E. Felder, A. Schilling, M. A. Chernikov, F. Hulliger, and H. R. Ott, Z. Phys. B **99**, 69 (1995).
[19] Y. Kawasaki, J. L. Gavilano, B. Roessli, D. Andreica, Ch. Baines, E. Pomjakushina, K. Conder, and H. R. Ott, J. Phys. Chem. Solids **69**, 3149 (2008).
[20] M. Chiao, S. S. Saxena, J. L. Gavilano, D. Rau, and H. R. Ott, J. Magn. Magn. Mater. **272-276**, 77 (2004).
[21] M. Weller, J. Hinderer, J. L. Gavilano, B. Pedrini, D. Rau, I. Sheikin, M. Chiao, and H. R. Ott, Physica B **378-380**, 829 (2006).
[22] E. Segal and W. E. Wallace, J. Solid State Chem. **2**, 347 (1970).
[23] S. Araki, N. Metoki, A. Galatanu, E. Yamamoto, A. Thamizhavel, and Y. Onuki, Phys. Rev. B **68**, 024408 (2003).
[24] P. G. Pagliuso, D. J. Garcia, E. Miranda, E. Granado, R. Lora Serrano, C. Giles, J. G. S. Duque, R. R. Urbano, C. Rettori, J. D. Thompson, M. F. Hundley, and J. L. Sarrao, J. Appl. Phys. **99**, 08P703 (2006).
[25] A. F. Garcia-Flores, J. S. Matias, D. J. Garcia, E. D. Martinez, P. S. Cornaglia, G. G. Lesseux, R. A. Ribeiro, R. R. Urbano, and C. Rettori, Phys. Rev. B **96**, 165430 (2017).
[26] A. C. Jacko, J. O. Fjærestad, and B. J. Powell, Nat. Phys. **5**, 422 (2009).
[27] G. W. Webb, F. Marsiglio, and J. E. Hirsch, Physica C **514**, 17 (2015).
[28] P. Hohenberg and W. Kohn, Phys. Rev. **136**, B864 (1964).
[29] P. Blaha, K. Schwarz, G. Madsen, D. Kvasnicka, and J. Luitz, *WIEN2k, An Augmented Plane Wave + Local Orbitals Program for Calculating Crystal Properties* (Technische Universitat, Wien, Austria, 2001).
[30] J. P. Perdew, K. Burke, and M. Ernzerhof, Phys. Rev. Lett. **77**, 3865 (1996).
[31] S. M. Young and C. L. Kane, Phys. Rev. Lett. **115**, 126803 (2015).
[32] C. Fang, Y. Chen, H. Y. Kee, and L. Fu, Phys. Rev. B **92**, 081201(R) (2015).
[33] C. Fang, H. Weng, X. Dai, and Z. Fang, Chin. Phys. B **25**, 117106 (2016).